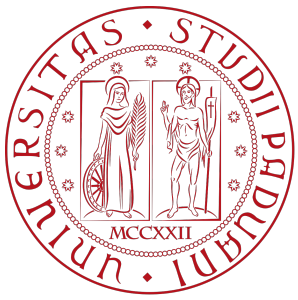

UNIVERSITÀ DEGLI STUDI DI PADOVA

Dipartimento di Fisica e Astronomia "Galileo Galilei"

Corso di Laurea in Fisica

Tesi di Laurea

Dynamic generation and detection of optical vortices by means of Spatial Light Modulators

Generazione dinamica e rilevazione di vortici ottici mediante Spatial Light Modulators

Relatore

Prof. Gianluca Ruffato

Laureando

Rugiada De Vallier

Anno Accademico 2021/2022

Abstract

A beam of light holds many properties such as the intensity value and spatial distribution, polarization (denoting spin angular momentum), wavelength (linear momentum), and orbital angular momentum (associated with its phase structure). Structured light refers to the control of these degrees of freedom, individually or in combination, in order to enhance or extend their optical capabilities. In the last decade, the possibility to modify and control the intensity and phase spatial distribution of light has fostered the applications of structured light beams in a wide range of fields, such as particle manipulation and tweezing, microscopy, imaging, classical and quantum communications. In this thesis, we analyze some of the most important families of structured light beams and how to control and measure their properties with the use of computer-controlled spatial light modulators (SLMs). An experimental optical setup based on SLMs has been arranged on an optical table and numerical codes have been developed for the generation of custom light beams carrying orbital angular momentum and their optical detection and analysis with holographic methods.

Un fascio di luce possiede molte proprietà quali l'intensità e la distribuzione spaziale, la polarizzazione (che denota il momento angolare di spin), la lunghezza d'onda (momento lineare) e il momento angolare orbitale (associato alla sua struttura di fase). Il termine luce strutturata fa riferimento al controllo di questi gradi di libertà, individualmente o combinandoli, al fine di potenziarne o estenderne le capacità ottiche. Negli ultimi dieci anni, la possibilità di modificare e controllare l'intensità e la distribuzione spaziale di fase della luce ha promosso le applicazioni dei fasci di luce strutturata in un ampio panorama di settori, quali manipolazione e intrappolamento di particelle, microscopia, imaging, comunicazioni classiche e quantistiche. In questa tesi, abbiamo analizzato alcune delle più importanti famiglie di fasci di luce strutturata e come controllarne e misurarne le proprietà mediante l'uso di spatial light modulators (SLMs). Un apparato ottico sperimentale basato su SLMs è stato predisposto su un banco ottico e codici numerici sono stati sviluppati per la generazione di specifici fasci di luce che trasportano momento angolare orbitale e per la loro rilevazione e analisi con metodi olografici.

Contents

Introduction

The concept of light beams carrying orbital angular momentum (OAM) is relatively recent in the history of physics even if optical vortices (OV) have been studied since 1970 [1]. The link between beams with helical wavefronts and orbital angular momentum had never been made until the 1990s. It was only in 1992 that Allen and collaborators found Laguerre-Gaussian(LG) laser modes to have well-defined orbital angular momentum. That work proposed and implemented the use of cylindrical lenses to transform the high-order Hermite-Gaussian modes emitted by a conventional laser into helically-phased LG modes [2].

From that moment forward, the field of beams carrying orbital angular momentum faced a cascade effect in the development of advanced topics in a wide range of fields. In the ten years going from 1898 to 1999, researchers focused their attention on understanding and developing fundamental theories and basic phenomena in order to pave the way for further studies and applications. From 1999 to 2009 many advances have been made in OAM manipulation and important applications started to emerge in the context of OAM-entangled photons [3], particle trapping and tweezing [4], microscopy and imaging [5] and more. The last ten years faced important progresses in advanced applications to high-capacity optical communication [6], quantum entanglement and single-photon applications with a high number of OAM states [7] and tunability of OVs at the nanoscale [8].

In this thesis, the main goals are represented by the generation and detection of beams carrying orbital angular momentum. In particular, once the principles of wave and beam optics have been underlined, the attention has been directed onto two classes of vortex beams: *perfect vortices* and *Laguerre-Gaussian beams*. Within the wide portfolio of methods developed to generate vortex beams, the diffractive approach based on the technology of *Spatial Light Modulators (SLMs)* has been selected and used in this work. In order to accomplish this goal, an optical setup based on SLMs has been arranged on an optical table. The collected images have allowed to visualize instantly the expected profile of the optical vortex beam and, with interferometric measurements, the orbital angular momentum carried. In a second moment, a comparison between the experimental data and the theory has been implemented by means of a *MATLAB* code. Subsequently, an in-depth discussion has been reserved to the possible approaches in order to detect OAM modes with different topological charges. Once the experimental setup has been properly re-arranged, different diffractive optical elements (DOEs) have been design by numerical codes and experimental data have been collected.

The thesis is structured as follows:

- Chapter 1: a brief derivation of the paraxial Helmholtz equation is presented, followed by the description of one of its most general and useful solution, i.e. the Gaussian beam, which is paradigmatic to introduce the features of a propagating optical beam. Right after, the concept of orbital angular momentum of light is introduced in order to underline the peculiar feature that characterizes OAM beams, the phase factor $exp(im\varphi)$. In conclusion, the more relevant classes of beams carrying OAM are introduced.
- Chapter 2: starting with an overview on the possible methods to generate vortex beams, a more detailed discussion is given for the more relevant approaches. It follows a description of the SLM technology, the one on which the thesis is focused. The chapter ends with the presentation of the experimental results. In particular, for both perfect vortices and LG beams different set

of data are shown to understand and observe the change of the beam shape depending on the variation of the control parameters.

- Chapter 3: the concept of mode-division (de)multiplexing (MDM) is discussed. After a brief introduction to underline the importance of this application, a more detailed treatment on the process to design diffractive optical elements is given. The chapter ends with the description of the experimental results collected in the laboratory: in particular, different holographic sorters have been generated in order to be loaded on an SLM for the detection of OAM modes in a range of different configurations, characterizing the optical performance in terms of efficiency and cross-talk.

Chapter 1

Vortex beams

Vortices are common phenomena in many fields of physics. In optics, an *optical vortex* is a point of zero intensity of an optical field, usually associated with a singularity, that can propagate along a beam which takes the name *vortex beam* or *optical vortex beam*. Such beams are powerful tools to study optical vortices, easily realized in the laboratory thanks to the important developments during the recent years. To analyse more in detail the features of vortex beams, it is recommended to start from the derivation of the possible analytic forms of vortex beams.

1.1 Helmholtz equation and paraxial approximation

In this context, light is described by the wavefunction $u(\vec{r},t)$, a scalar real function of position and time, that obeys the wave equation

$$\nabla^2 u - \frac{1}{c^2}\frac{\partial^2 u}{\partial t^2} = 0 \tag{1.1}$$

The simplest solution is the monochromatic wave $u(\vec{r},t) = a(\vec{r})cos[\varphi(\vec{r}) - \omega t]$ which is useful to write in complex notation so that,

$$u(\vec{r},t) = \Re\{U(\vec{r},t)\} = \frac{1}{2}[U(\vec{r},t) + U^*(\vec{r},t)]$$

The complex wavefunction $U(\vec{r},t)$ can be written as $U(\vec{r},t) = U(\vec{r})exp(-i\omega t)$ in which $U(\vec{r})$ is the complex amplitude of the wave. Writing the wave equation in term of the complex wavefunction the Helmholtz equation is obtained,

$$\nabla^2 U + k^2 U = 0 \tag{1.2}$$

where $k = 2\pi/\lambda$ is the wavevector modulus. This is the starting point to derive the analytic forms of light beams carrying orbital angular momentum, that are our object of interest.

Plane and spherical waves are the simplest solutions of the Helmholtz equation but they present some limits in term of confinement: the first propagates in one direction but the energy extends over the entire space, the second originates from a single point but diverges in all directions.

In this discussion the interest is addressed to optical beams, electromagnetic waves that remain essentially concentrated around a well defined direction upon free propagation. It derives the necessity to find a solution that can describe a wave that propagates with wavefront normals that make small angles with the propagation direction. These waves are called paraxial waves and they are characterized by a complex envelope $A(\vec{r})$ which is a slowly varying function of the position z: $U(\vec{r}) = A(\vec{r})exp(ikz)$.

From the substitution of this definition into the Helmholtz equation it follows that,

$$\nabla_{\perp}^2 A + \frac{\partial^2 A}{\partial z^2} + 2ik\frac{\partial A}{\partial z} = 0$$

To maintain the underlying plane-wave nature, the variation of the envelope A and its derivative with z must be slow within the distance of a wavelength, which implies

$$\left|\frac{\partial A}{\partial z}\right| << |kA| \qquad \left|\frac{\partial^2 A}{\partial z^2}\right| << \left|k\frac{\partial A}{\partial z}\right| \qquad \left|\frac{\partial^2 A}{\partial z^2}\right| << \left|\nabla_{\perp}^2 A\right|$$

It follows the equation for the complex envelope,

$$\nabla_{\perp}^2 A + 2ik\frac{\partial A}{\partial z} = 0$$

which is known as *paraxial Helmholtz equation.*

The simplest solution is the paraboloidal wave, which is an approximation of the spherical wave in the paraxial approximation; however, a more general and powerful solution is the Gaussian beam.

1.1.1 The Gaussian beam and its features

The Gaussian beam's complex envelope is given by

$$A(\vec{r}) = \frac{A_0}{q(z)} exp\left[- ik\frac{\rho^2}{2q(z)}\right]$$

where the complex quantity *q(z)* is called the q-parameter and is defined as $q(z) = z + iz_{_R}$. The Rayleigh range $z_{_R}$ quantifies the length over which the beam can propagate without diverging significantly. To separate amplitude and phase terms, it is useful to introduce two other real functions $R(z)$ and $w(z)$, the wavefront curvature radius and the beam radius respectively, both dependent on the coordinate z:

- $R(z) = \dfrac{z^2 + z_{_R}^2}{z}$ is the radius of curvature as a position of z along the beam axis.
- $w(z) = w_0\sqrt{1 + \left(\dfrac{z}{z_{_R}}\right)^2}$ is the radius of the circle within which the 86% of the total power is carried. It is called beam radius and it assumes its minimum value at $z = 0$, that corresponds to $w_0 = \sqrt{\dfrac{\lambda z_{_R}}{\pi}}$, the beam waist radius. The beam width increases monotonically with z and assumes the value $\sqrt{2}w_0$ at $z = \pm z_{_R}$.

Rewriting the complex envelope in term of $R(z)$ and $w(z)$:

$$\frac{1}{q(z)} = \frac{1}{z + iz_{_R}} = \frac{1}{R(z)} - i\frac{\lambda}{\pi w^2(z)}$$

Then the complex amplitude acquires the form:

$$U(\vec{r}) = A_0\frac{w_0}{w(z)} exp\left[- \frac{\rho^2}{w^2(z)}\right] exp\left[ikz - ik\frac{\rho^2}{2R(z)} + i\zeta(z)\right]$$

in which,

- $A_0 = A_1/(iz_R)$ defined in this way for the convergence, where A_0 and z_R are determined by initial conditions
- $\zeta(z) = \tan^{-1}\left(\frac{z}{z_R}\right)$ is the Gouy phase that represents the phase retardation with respect to a plane wave, due to the focusing of the beam at the beam waist

The intensity of the Gaussian beam is given by $I(\rho, z) = |U(\rho, z)|^2$. It assumes its peak on the beam axis, then decreases as $1/e^2$ at the radial distance $w(z)$.

1.2 Orbital angular momentum of light

The total angular momentum is the vectorial sum of the spin angular momentum (SAM) and the orbital angular momentum (OAM). More precisely, the former is related to the twisting polarization and it takes an important role in the vectorial framework of electromagnetism, while the latter, related to the rotating wavefronts, is that taken into account in the discussion of light beams carrying orbital angular momentum. Hence, even if a great number of solutions for the paraxial Helmholtz equation are known, the ones considered here are those with a phase factor $exp(im\varphi)$, that indicates the existence of an optical vortex, a phase singularity appearing as a dark spot.
In these beams, light is twisted around the axis of propagation generating helical phase fronts from which the typical annular intensity cross-section originates. The integer m, known as *topological charge*, defines the features of orbital angular momentum beams: its absolute value gives the number of intertwined helical wavefronts, while the sign gives the chirality of the helices. Considering light as composed of photons, the topological charge also represent the quantity of orbital angular momentum carried per photon in units of $\hbar$ and each value of m corresponds to a state orthogonal to all the others. This is a powerful tool in the field of optical communications in order to increase the number of channels or the Hilbert state space of photons.

1.2.1 Solutions to the paraxial Helmhotz equation

An exact solution of the full Helmholtz equation in cylindrical coordinates is provided by Bessel beams:

$$U_\kappa^m(\rho, \varphi, z) = J_m(\kappa\rho)e^{im\varphi}e^{ikz}$$

where J_m is the Bessel function of the first kind of order m. These solutions are useful for the analysis of the propagation of beams with OAM in the non-paraxial regime; however, having an infinite transverse profile they cannot be physically generated. More realistic beams are represented by Bessel-Gaussian beams that are endowed with a Bessel-like intensity profile modulated by a Gaussian term:

$$U_\kappa^m(\rho, \varphi, z) = J_m(\kappa\rho)exp\left(\frac{-\rho^2}{w_0^2}\right)e^{im\varphi}e^{ikz}$$

Another important class of beams which is related to Bessel beams can be obtained applying the Fourier transform for input Bessel beams,

$$U(r, \varphi) = \frac{1}{\kappa}i^{m-1}e^{im\varphi}\delta(r - R)$$

This describes a *perfect vortex* with charge m and radius $R = \frac{\kappa f}{k}$, being f the focal length used to implement the Fourier transform in the f-f configuration. In particular, due to the characteristics of Bessel functions, this form is not useful for experimental intentions. A more realistic case is that of real perfect vortices, which originates from Bessel-Gaussian beams, and take the form

$$U(r, \varphi) = \frac{w_0}{w_R}i^{m-1}e^{im\varphi}exp\left[-\frac{(r - R)^2}{w_R^2}\right]$$

This is a realistic perfect vortex with radius $R = \frac{\kappa f}{k}$ and width $w_R = \frac{2f}{kw_0}$; the significant characteristic of these beams is that the radius does not depend on the charge m.
Laguerre-Gaussian modes provide a complete set of solutions to the paraxial Helmholtz equation, in cylindrical coordinates:

$$U_p^m(\rho,\varphi,z) = A_p^m \frac{w_0}{w(z)} \left(\frac{\sqrt{2}\rho}{w(z)}\right)^{|m|} L_p^{|m|}\left(\frac{2\rho^2}{w^2(z)}\right) exp\left(-\frac{\rho^2}{w^2(z)}\right) exp\left(-ik\frac{\rho^2}{2R(z)}\right) e^{i(2p+|m|+1)\zeta(z)} e^{im\varphi} e^{ikz} \tag{1.3}$$

where L_p^m are the associated Laguerre polynomials and $A_p^m = \sqrt{\frac{2p!}{\pi(p+|m|!)}}$.
Each mode is identified by a couple of indices (p, m): the azimuthal index m represent the orbital angular momentum, the radial index p gives the number of radial nodes, and so the number of concentric rings, $p+1$. The radius is proportional to $\sqrt{|m|}$ as, $R(z) = w(z)\sqrt{\frac{|m|}{2}}$.

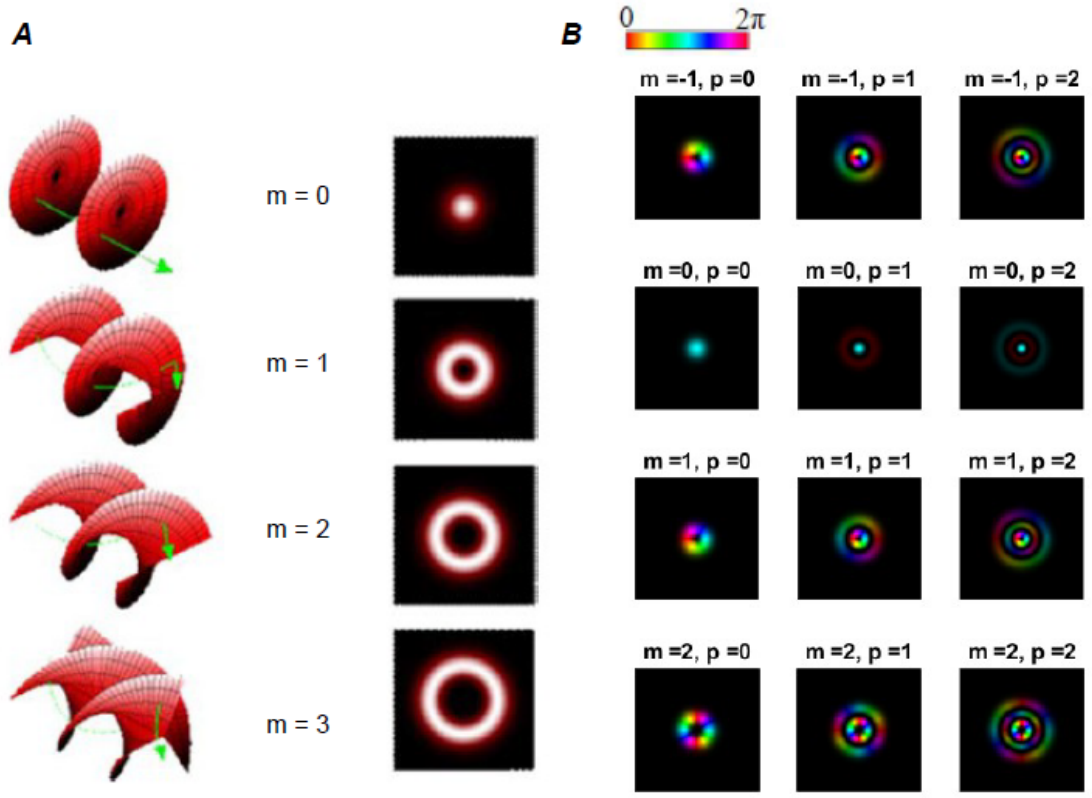

Figure 1.1: evolution of helical wavefronts for different OAM beams with relative intensity profile with $p = 0$ (A), phase distribution for LG beams with different topological charge m and azimuthal index p (B)

Chapter 2

OAM beams generation

The possibility to generate optical vortex beams has been explored before the link between the peculiar features of these beams and orbital angular momentum was made.
The most relevant work in this perspective has been that of Soskin and co-workers in 1990 [9]. They used diffraction grating containing m-pronged fork dislocations coaxially aligned with an incident plane-waved beam that, in a first-order approximation, emerged as a diffracted beam with helical wavefronts described by the phase factor $e^{im\varphi}$.

On the other side, in 1993, Allen *et al* developed the use of converters in order to transform an Hermitte-Gaussian mode, indexed by i and j, into a Laguerre-Gaussian mode, L_p^m, with the relations $m = (i-j)$ and $p = min(i, j)$. The input beam can be seen as a decomposition into different HG modes that are re-phased by changing the Gouy phase shift by means of a proper converter, $\pi/2$-converter, made up by two cylindrical lenses. This method takes the name of *Astigmatic mode conversion with cylindrical lenses*; it has high efficiency and offers a near lossless transformation between HG and LG modes, but, on the other side, requires high construction precision and has poor flexibility because it needs accuracy in the specification or alignment of the cylindrical lenses to avoid any residual astigmatism in the resulting LG mode [10].
Another approach to generate vortex beams consists in using some optical components denoted as *Spiral Phase Plates*, spiraling steps with a refractive index n whose thickness increases with the azimuthal angle. The step height is given by $h = (m\lambda\theta)/(2\pi(n - n_0))$, being n_0 the refractive index of the surrounding. When light passes through the phase plate it experiences a different phase in the azimuthal direction and is converted into a helically phased beam with topological charge m. This type of conversion avoids the risk of astigmatism, the efficiency is still high and can be used with high power laser beams, but there are some limits in the number of modes that can be generated and imposes extremely high requirements on technical tolerance, especially with regard to optical wavelengths [11].
Some other devices employed in the generation of OAM beams are *q-plates* [12]and metamaterials. The former are liquid crystal films having a uniform birefringence phase retardation and a transverse optical axis pattern with a non-zero topological charge. *Q-plates* are based on the SAM-OAM coupling; these tools are able to produce a pure OAM mode, but there is a limit represented by the energy threshold being made of liquid crystals. *Metamaterials* are planar ultra-thin optical components that operate forcing a sudden change of some features of an incident beam, like phase, amplitude and polarization. The OAM beam is obtained by controlling the geometrical parameters of the metamaterial. These tools have the advantage of the small size that allows easy integration, but, at the same time, are limited in producing only one mode for a single device in a versatile and dynamic way.

Nowadays, despite the great number of different methods for generating vortex beams, in the majority of the modern experiments a diffracting-optics approach is preferred since holographic diffraction gratings are simple and fast to produce and have high efficiency; however, only low-order vortex beams can be generate because their quality is seriously degraded while increasing the number of diffraction orders. These diffractive-optical elements can be produced by *Spatial Light Modulators*

that allow to generate different OAM modes using a single device.

2.1 Spatial light modulators technology

A *Spatial Light Modulator (SLM)* is a device consisting in a pixelated display, formed by several hundreds of thousands cells, that allows to modulate or manipulate some properties of light. Each cell is filled with Liquid Crystals (LC), a state of matter that has properties between those of conventional liquids and those of solid crystals. Under appropriate conditions LC molecules tend to align in a preferred direction. Depending on the molecular order or organizational constraints, it's possible to classify LCs in nematic, smectic or cholesteric. In the first case all the molecules have the same orientation but are randomly located. In the second one there is a certain degree of positional order and the molecules are arranged in layers. In the last one the molecules show an helix-like layered structure.
The technology of SLMs is based on LCs properties implemented upon reflection or transmission from which two classes of possible devices derive: transmissive type uses transparent LC displays (LCDs), while reflective one uses liquid crystal on Silicon displays (LCoS). A LCoS display consists in a Silicon substrate covered with pixelated metal electrodes which control LC molecules in each cell. The thin layer of LC is sandwiched between two alignment films above the active matrix circuit of electrodes, and upon the upper film another layer of transparent electrode is posed. The whole system is finally covered by a flat glass substrate (figure 2.1). SLMs act like a second monitor controlled by the

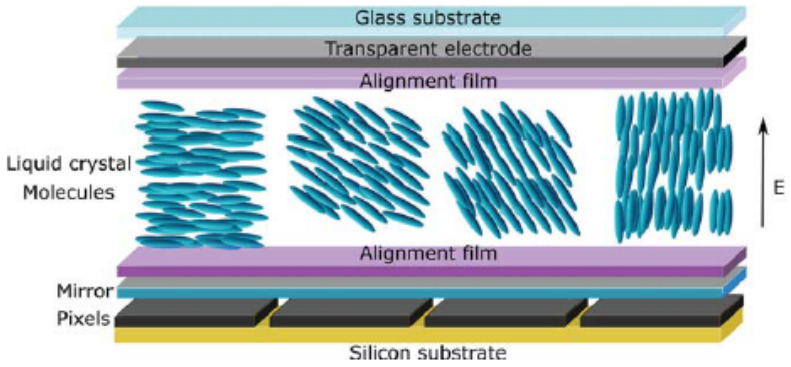

Figure 2.1: Scheme of an SLM cross-section

computer; the working principle consists in finding an appropriate image, called computer-generated hologram, that produces the required result. The grayscale of the image, in which each level of grey is associated with a discrete increment of the phase from 0 (black) to 2π (white), is used to control the LCs in each pixel and therefore to modulate the phase of any light beam interacting with it, with micrometric resolution. At this point, it is possible to appreciate the flexibility of SLM in the sense that it is not required a specific software to control the pixeled array, it is only necessary to have the image of the digital hologram designed in a scale of grey that, once it is uploaded on the SLM, is converted into a voltage scale to obtain the desired phase modulation.

2.1.1 Phase and Amplitude modulation

The conversion from the greyscale and the desired phase change is not automatic and needs some precautions. In general to create structured light modes it is necessary a transmission function with both phase and amplitude modulation. Considering the complex field we want to generate:

$$U(x,y) = A(x,y)e^{i\varphi(x,y)}$$

it is needed a phase-only field that incorporates both amplitude and phase variation; this is required by most modern SLMs that are phase-only devices. In order to do that a function $h(x,y)$ is defined as,

$$h(x,y) = e^{if(A)sin\varphi(x,y)}$$

By applying the Jacobi-Anger expansion we obtain,

$$e^{if(A)sin\varphi(x,y)} = \sum_{n=-\infty}^{\infty} J_n(f(A))e^{in\varphi(x,y)}$$

where J_n is the nth-order Bessel function of the first kind. The first order $J_1(f(A))e^{i\varphi(x,y)}$ is sufficient to define properly the function f in order to satisfy the relation: $J_1(f(A)) = A$. To spatially separate the different orders result, a tilt term βx is added to the phase function $\varphi(x, y)$.

Before going into the details of the experimental generation of beams carrying OAM, it is important to underline that despite the high flexibility and high dynamical control, SLMs are not 100% efficient as a result of pixelation. Moreover they are relative expensive and have a low resolution.

2.2 OAM beams generation

In the next sections the generation of *perfect vortices* and *Laguerre-Gaussian beams* is discussed in details.

2.2.1 Experimental setup

In order to accomplish this purpose an experimental setup based of SLMs is set on an optical table (figure 2.2,figure 2.3).

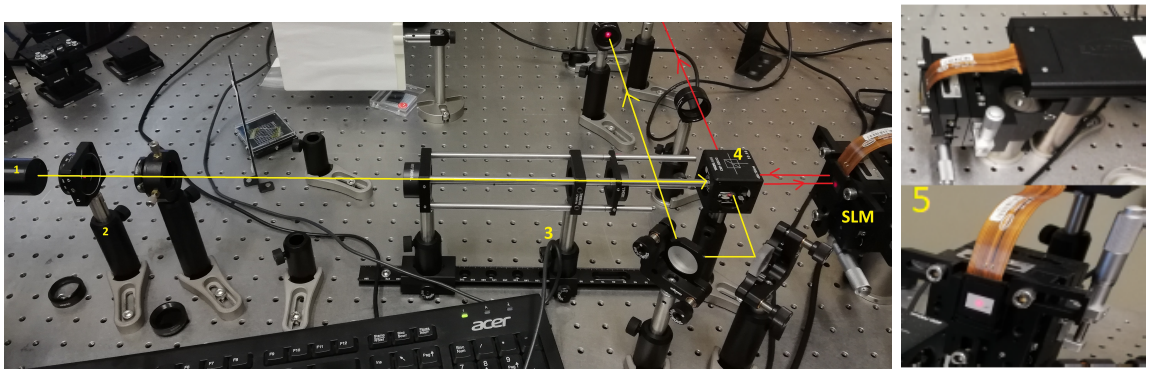

Figure 2.2: Optical line before SLM: 1.laser, 2.polarization filter, 3.telescope, 4.beam splitter, 5.SLM

The source of light is a laser of wavelength $\lambda = 632.8\,nm$ (HeNe laser, HNR008R, Thorlabs). This is followed by a horizontal polarization filter and a telescope made by two lenses with focal length $d_1 = 2.54\,cm$ and $d_2 = 15\,cm$ respectively, resulting in a magnification equal to the ratio d_2/d_1. After the telescope a beam splitter 50 : 50 divides the beam into two parts: one goes straight until the SLM, the other remains unperturbed and it is redirected by a sequence of mirrors for interferometry analysis. The SLM used (PLUTO-NIR-010-A, Holoeye) has a reflective LCoS display with a resolution of 1920x1080 pixels which have a pitch of 8 μm, 8-bit depth (256 phase levels) (figure 2.2).

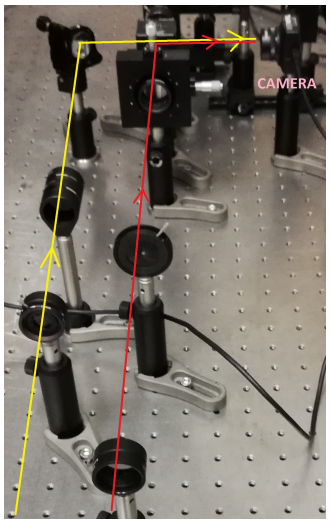

Figure 2.3: Optical line after SLM

After interacting with the SLM, the emerging beam includes the desired optical vortex. In the view of isolating and imaging only the first order, a $4f$ system with an aperture in the Fourier plane is set. This system consists of two lenses with focal length $f_1 = 20\,cm$ and $f_2 = 25\,cm$ respectively, placed at a distance $d = f_1 + f_2 = 2f$, the SLM at a distance f_1 from the first lens, the detecting camera that completes the optical line at a distance f_2 from the second lens and an iris in the middle of the two

lenses that removes all the orders except for the first one. The DCC camera (DCC1545M, Thorlabs) detects also the unperturbed beam, in this way it is possible to observe explicitly the topological charge of the structured light beam thanks to their interference (figure 2.3).

The first step in order to generate beams carrying orbital angular momentum is the realization of a computer-generated hologram with the phase and amplitude modulation described in section 2.1.1. To generate them some *MATLAB* codes have been used.

2.2.2 Perfect vortices

As seen, a *perfect vortex beam* is characterized for having a beam radius that doesn't depend on the topological charge m. After setting up $w_R = 0.8\,mm$, $R = 1.1\,mm$ and the topological charge in the interval $m = [-5; 5]$, the resulting holograms have been uploaded by a specific program on the SLM.

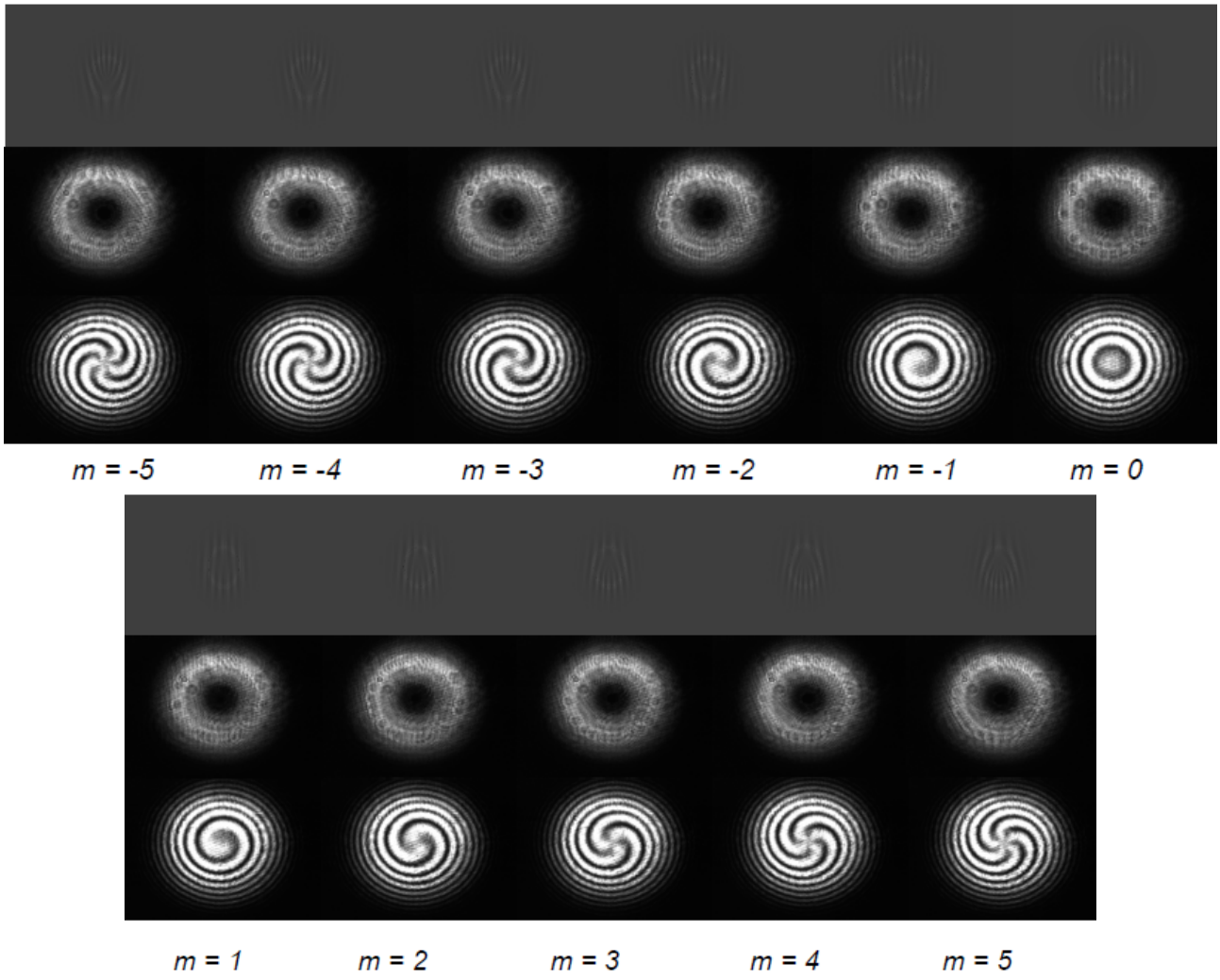

Figure 2.4: Perfect Vortices: SLM holograms (first row), intensity profiles (second row), spiral interferograms (third row)

In figure 2.4 first row, it is possible to observe the computer-generated holograms in the greyscale that are converted in voltage variations by the electronic circuit of the SLM. In the central rows of images the characteristic "donut" shape allows to underline the independence of the beam radius from the topological charge. As predicted by the theory, the intensity profile shows a black hole in the centre because of the phase singularity. In the third row the result of the interference between the vortex beam and the unperturbed, that is a Gaussian, is show: the result is a spiral interference pattern that underlines the shape of the wavefronts that are helically twisted around the axis of propagation, with the number of helices and the verse of rotation given respectively by the modulus and the sign of the topological charge.

To confirm that the beams generated are actually the desired ones, a *MATLAB* code has been implemented to compare the theoretical expectation, seen in section 1.2.1, with the experimental result. Taking a fixed radius, the intensity averages along concentric circles are plotted in order to observe the intensity profile in the interval $[0; R']$, where $R' = \frac{5}{4}R$ due to the magnification of the telescope.

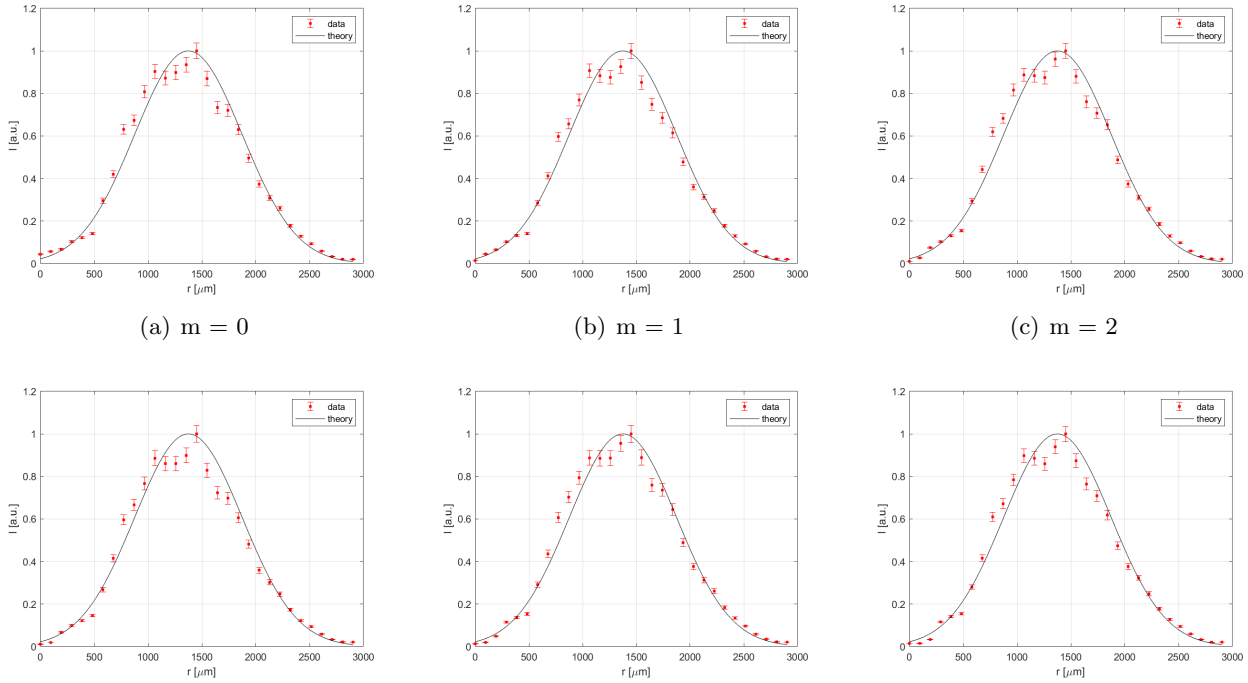

(a) m = 0 (b) m = 1 (c) m = 2

(d) m = 3 (e) m = 4 (f) m = 5

Figure 2.5: Comparison between theoretical function of perfect vortices and experimental results

Figure 2.5 shows how the experimental data follow up effectively the theoretical law seen in section 1.2.1. Data around the peak are characterized for a large error because of the low resolution of the SLM that introduces noise in the generation of the beam.

This procedure has been repeated taking a fixed value $m = 5$ and varying the parameters w_R and R to observe the way in which the profile of the vortex changes (Table 2.1).

Perfect vortices with m = 5

	w_R	R
a	0.1 mm	0.2 mm
b	0.1 mm	0.4 mm
c	0.3 mm	0.4 mm
d	0.2 mm	0.8 mm
e	0.4 mm	0.8 mm
f	0.5 mm	1.2 mm

Table 2.1: Parameters w_R and R for different *perfect vortices* with fixed m = 5

In figure 2.6 the detected images are collected and, as previously done, the experimental data and the model have been compared to confirm that the beams generated were those desired.

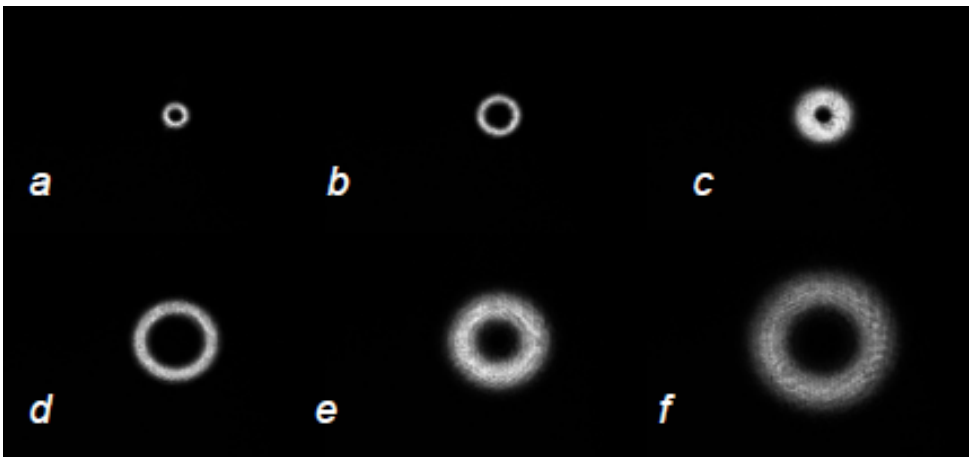

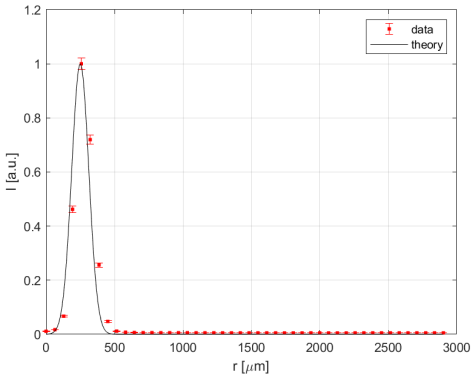

(a) $R = 0.2\,mm$, $w_R = 0.1\,mm$

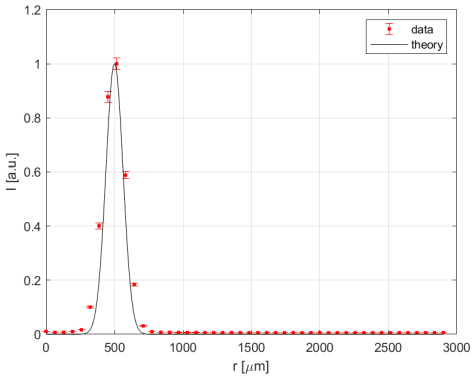

(b) $R = 0.4\,mm$, $w_R = 0.1\,mm$

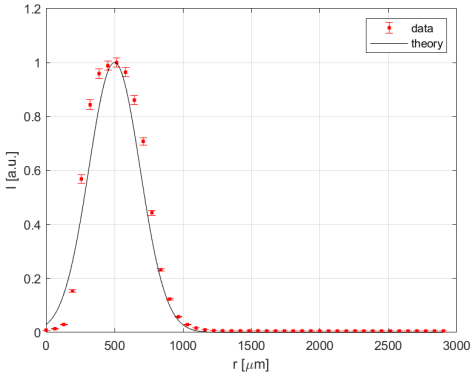

(c) $R = 0.4\,mm$, $w_R = 0.3\,mm$

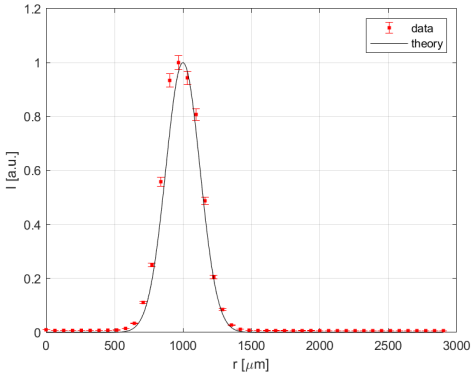

(d) $R = 0.8\,mm$, $w_R = 0.2\,mm$

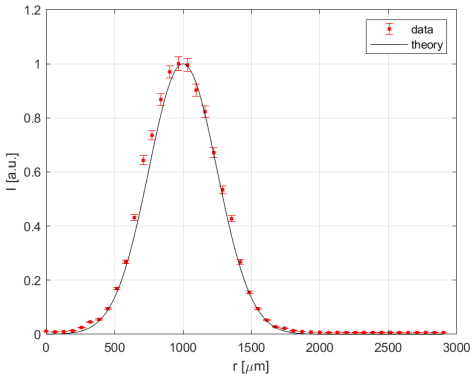

(e) $R = 0.8\,mm$, $w_R = 0.4\,mm$

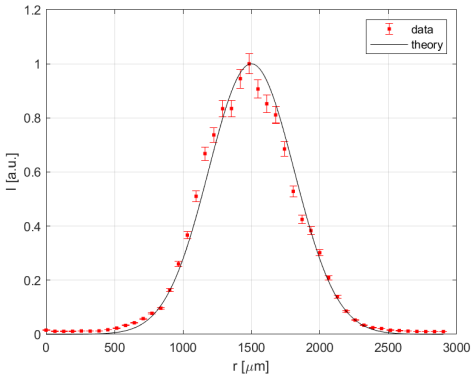

(f) $R = 1.2\,mm$, $w_R = 0.5\,mm$

Figure 2.6: Perfect Vortices at fixed m, different radius and width, and comparison with theory. The experimental maximum radius is $R' = 5/4R$, as expected, due to the telescope magnification.

2.2.3 Laguerre-Gaussian beams

As seen in section 1.2.1, the parameter that is possible to control in LG beams is the beam waist, w_0, from which the beam radius R depends. Once configured the desired $w_0 = 0.8\,mm$, the values of the topological charge m and the azimuthal index p have been varied in the code for the generation of the computer-generated holograms. Firstly, the azimuthal index p has been set at the value $p = 0$, to focus the attention on the variation of the intensity profile due to the change of the topological charge.

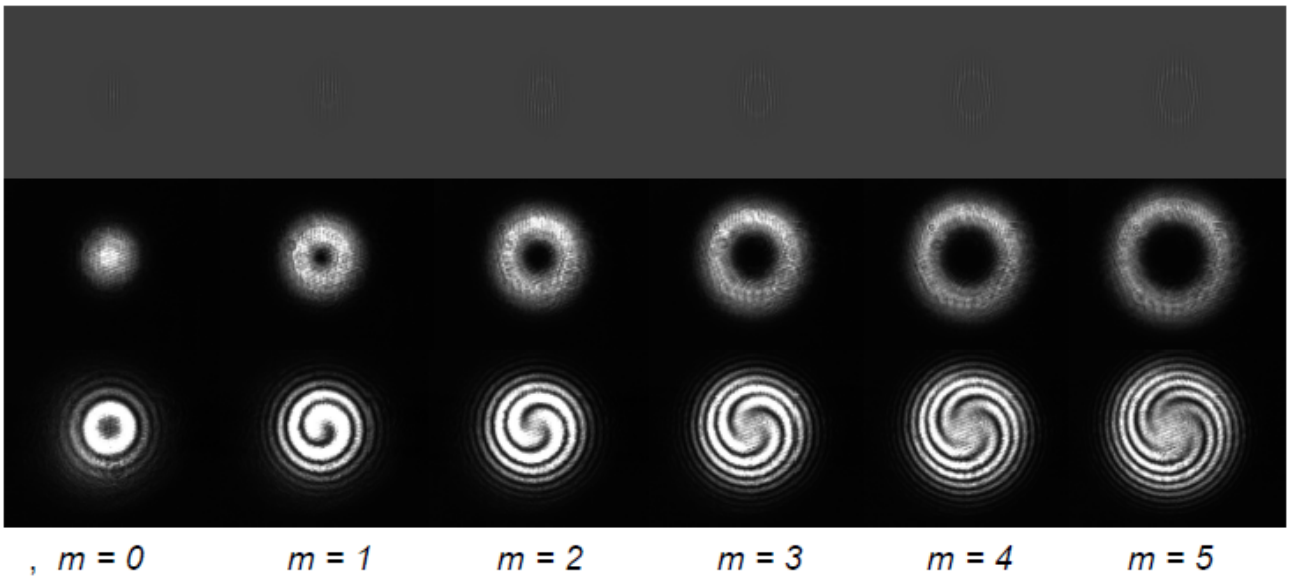

Figure 2.7: Laguerre-Gaussian beams: SLM holograms (first row), intensity profiles (second row), spiral interferograms (third row)

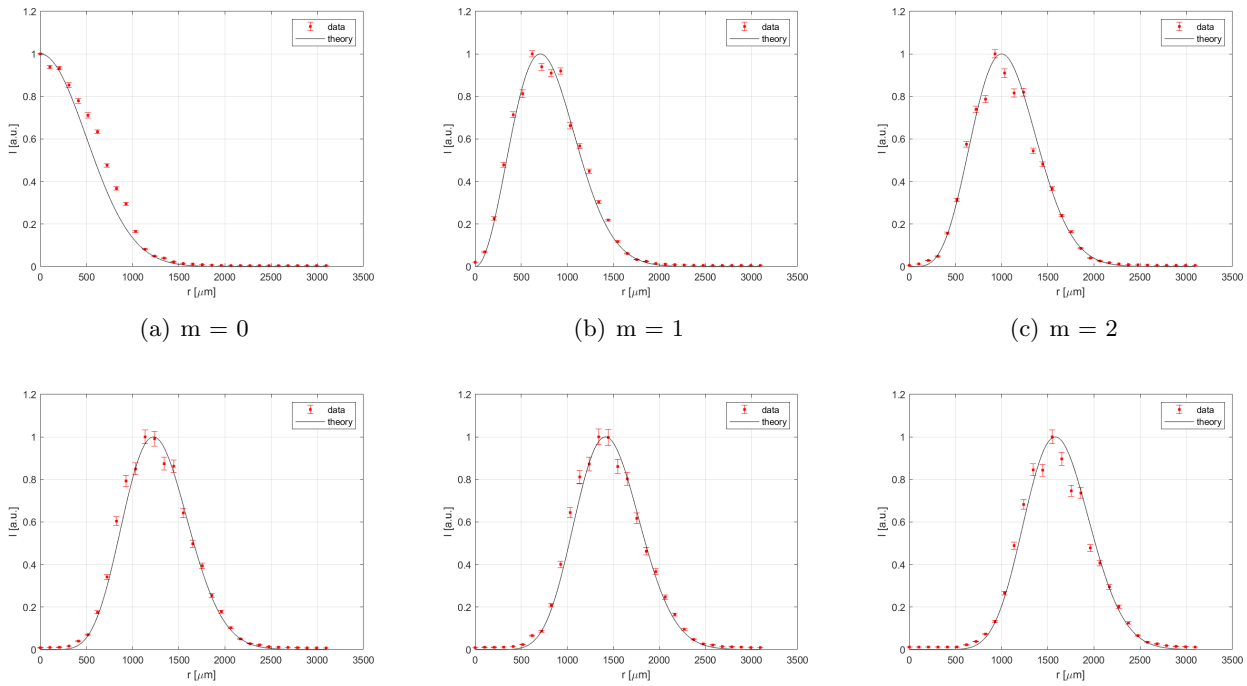

(a) m = 0 (b) m = 1 (c) m = 2

(d) m = 3 (e) m = 4 (f) m = 5

Figure 2.8: Comparison between theoretical profiles of Laguerre-Gaussian beams (eq.1.3) and experimental results

In figures 2.7 and 2.8, it is possible to appreciate the increase of R depending on m. The first image in the second row is simply a Gaussian beam and it doesn't show the phase singularity of the optical vortex because for $m = 0$ the beam doesn't carry OAM. In the last row the spiral interferograms permit to visualize the helical wavefronts due to the orbital angular momentum imposed. Also in this case a *MATLAB* code has been implemented to compare the experimental result with the theoretical expectation (figure 2.8).

In a second moment, beams with $p \neq 0$ have been generated. In specific, the values $m = 1, 2, 3$ and $p = 0, 1, 2$ have been taken into account. The resulting vortex beams are collected in the following figure.

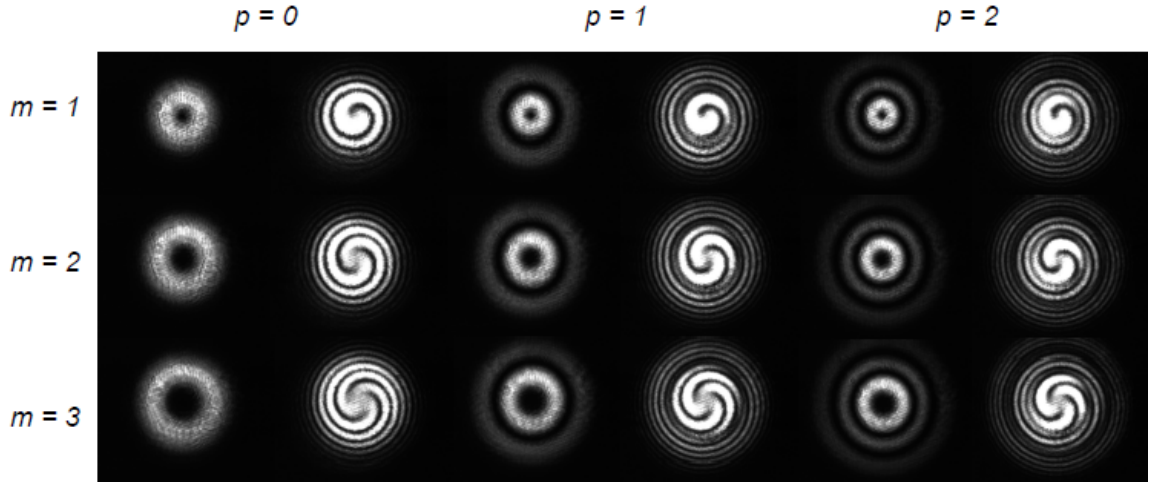

Figure 2.9: Laguerre-Gaussian beams with variable p: intensity profile and spiral interferograms

In figure 2.9, it's possible to see the increase in the number of rings, varying the azimuthal index, related to the forms of the polynomials of Laguerre in eq.1.3. In the spiral interferograms the presence of the index p results in a phase shift π that is possible to see looking at the helices which are not continuous in brightness. Also for these cases, a comparison between experimental data and theory has been implemented. The results are collected in the following figures.

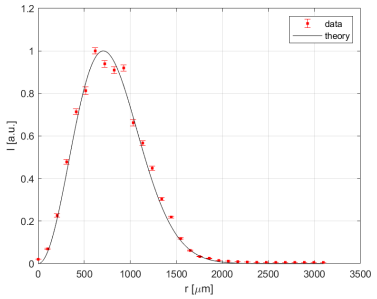

(a) p = 0

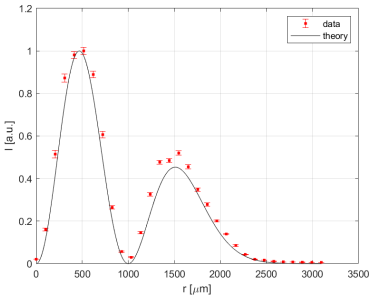

(b) p = 1

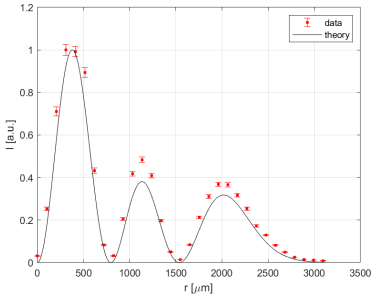

(c) p = 2

Figure 2.10: Comparison between theoretical function of LG beams and experimental results (m=1)

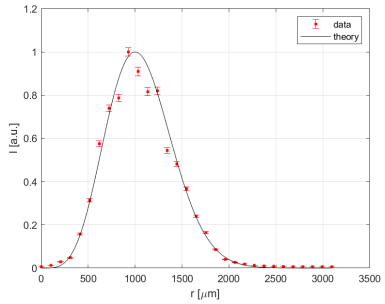

(a) p = 0

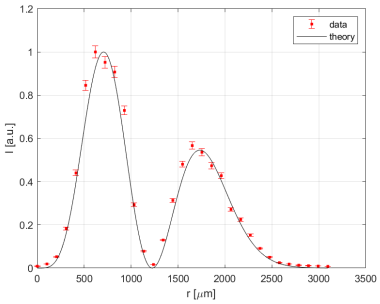

(b) p = 1

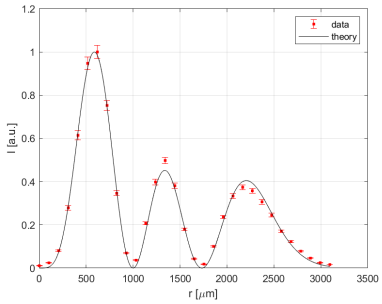

(c) p = 2

Figure 2.11: Comparison between theoretical function of LG beams and experimental results (m=2)

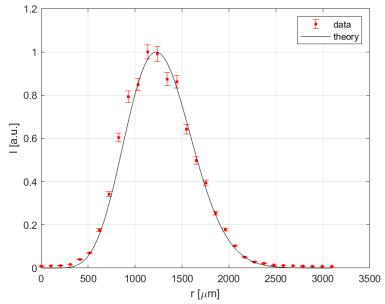

(a) p = 0

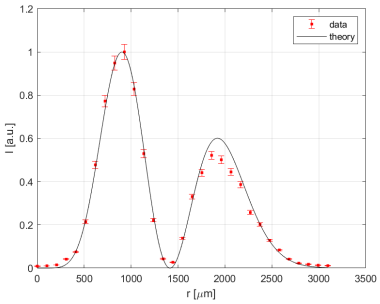

(b) p = 1

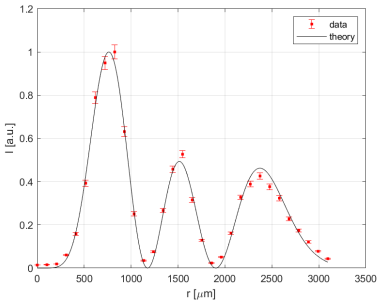

(c) p = 2

Figure 2.12: Comparison between theoretical function of LG beams and experimental results (m=3)

Chapter 3

Detection of optical vortices

One of the fields in which increasing attention is given to vortex beams is that of telecommunications. Nowadays the information transmission capacity has almost reached the physical limit of single-mode optical fibers, the so-called Shannon limit [13]; consequently, the request of alternative transmission methods becomes relevant. In this perspective, the orbital angular momentum of light suggests the possibility of multi-mode transmission thanks to the orthogonality of different OAM beams. This technique takes the name of mode division (de)multiplexing (MDM). Different procedures exist in order to sort a set of multiplexed different OAM beams. The diffractive optics approach, consisting in the use of holographic OAM-mode analyzers, is the one considered in this thesis.

3.1 Diffractive OAM-mode analyzers

The key point of this method is the proper design of a diffractive optical element (DOE) that is based on a harmonic analysis consisting in an expansion of the incident beam into a linear combination of angular harmonics. The phase pattern is described by a transmission function written as linear combination of a selected number of element of the chosen orthogonal basis $\psi_j \propto \exp(im\theta)$, resulting as

$$\Omega_{DOE}(\rho,\theta) = \arg\left\{\sum_{j=1}^{n} c_j \psi_j^* \exp[i\rho\beta_j cos(\theta-\theta_j)]\right\}$$

where $\{(\beta_j,\theta_j)\}$ are the vectors of the carrier spatial frequencies in polar coordinates and c_j are the complex coefficients given by the relation

$$c_j = \int_0^{2\pi} d\theta \int_0^{\infty} \psi_j \exp(i\Omega_{DOE}) \exp[-i\rho\beta_j cos(\theta-\theta_j)]\rho d\rho$$

The modulus of c_j is given arbitrarily while the relative phases are free parameters of the task. In order to calculate this phase pattern for a given basis of OAM modes with topological charges $\{m_j\}$ an iterative algorithm based on a modified Gerchberg-Saxton method implemented in *MATLAB* is used. The algorithm [14] consists in computing the sums in the transmission function $\Omega_{DOE}(\rho,\theta)$ and the integrals of the coefficients c_j using the Fast Fourier Transform algorithm (FFT) imposing some constraints: at the p-th iteration, the coefficient $c_j^{(p)}$ is replaced by $c_j^{*(p)}$ with

$$c_j^{*(p)} = \left[\gamma T_j + (1-\gamma)|c_j^{(p)}|\right] \frac{c_j^{(p)}}{|c_j^{(p)}|}$$

where $0 < \gamma \leq 2$ and $T_j = 1$ are the relaxation coefficient that controls the convergence and pre-given numbers characterizing the response of each channel respectively. The resulting estimation is put in the transmission function, after phase quantization is applied. At the end, the resulting DOE is assumed to be fabricated as surface-relief patterns of pixels realized, for example, by electron beam lithography (EBL). In the framework of this thesis, the designed phase patterns have been loaded onto an SLM as Bitmap figures.

3.2 Holographic sorter by means of SLM

In order to observe different configurations in detecting OAM beams, an important role is assumed by SLMs, due to their flexibility in using only one device to model different samples, but with a loss in terms of resolution. In the following sections, demultiplexing and detection of *perfect vortices* with $R = 0.8\,mm$ and $w_R = 0.3\,mm$ are discussed in details.

3.2.1 Experimental setup

The experimental setup used is that exposed in section 2.2.1 with the addition of some elements at the end of the optical line.

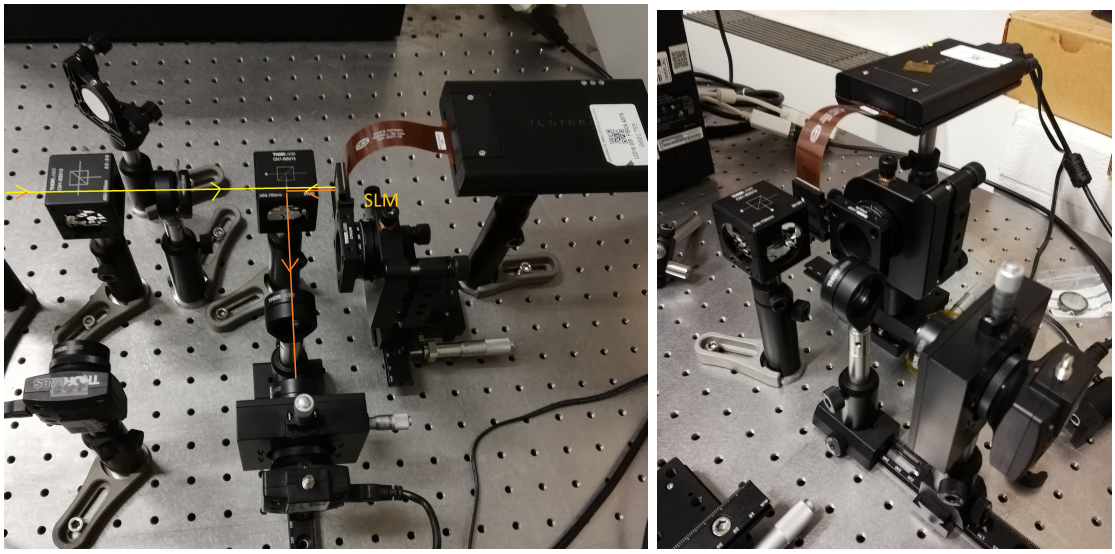

Figure 3.1: Experimental setup and SLM for optical vortex beams detection

In particular, the OAM beam generated by means of the first SLM is directed through the last beam splitter into a system composed by an SLM identical to the first one (PLUTO-NIR-010-A, Holoeye), a DCC camera (DCC1545M, Thorlabs) and a lens in between the two, of focal length $f = 12.5\,cm$ placed at a distance $d = f$ from both the DCC camera and the SLM (figure 3.1)

Once the optical setup is composed, *MATLAB* codes are used to produce different types of phase patterns. These are realized modifying the sequence of coding lines in which the parameters r_j and ϕ_j, defining the positions of the spots (r_j, ϕ_j) in the far-field, are set: the relation with the vectors $\{(\beta_j, \theta_j)\}$ is given by,

$$\begin{cases} r_j = \beta_j \dfrac{f}{k} \\ \phi_j = \theta_j \end{cases}$$

In particular, the attention is focused on three aspects: the spatial configuration, the selection of the number of different OAM modes and the choice of subsequent topological charges. In the following, we will consider the effect of changing these degrees of freedom in the sorter design.

3.2.2 Design of the spatial configuration

The values of topological charge taken into account in this case are $m = [-3; 3]$. The general procedure has been the following: at first the coordinates r_j and θ_j are set in order to visualize different configurations for the detection spots: in particular, a straight line and an exponential spiral have been considered. Once the phase patter is produced, as described in the previous section, it has been loaded on the second SLM accepting the OAM beam generated by the first one. At this point the reflected beam is directed to the camera in order to visualize and collect the result.

- **Bisector configuration**

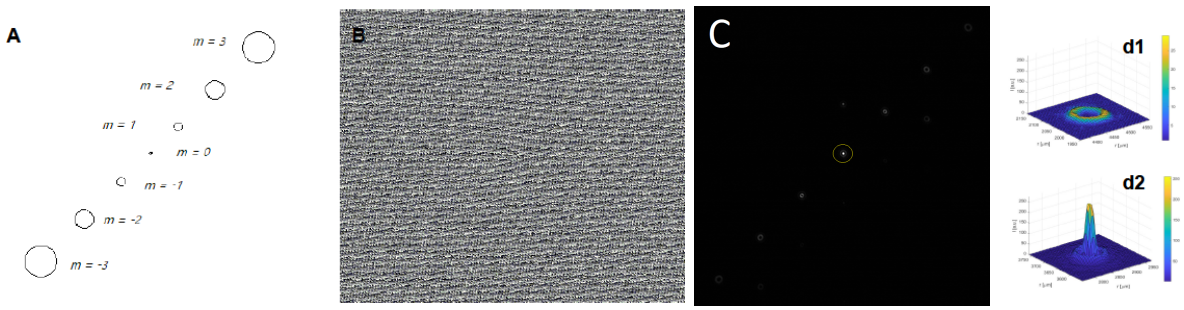

Figure 3.2: bisector configuration model(A), designed DOE(B), DCC image (C), 3D plots of a hole (d1) and a peak(d2) in the far-field. The thin yellow circle surrounds the region in which the detector of the selected OAM beam is located.

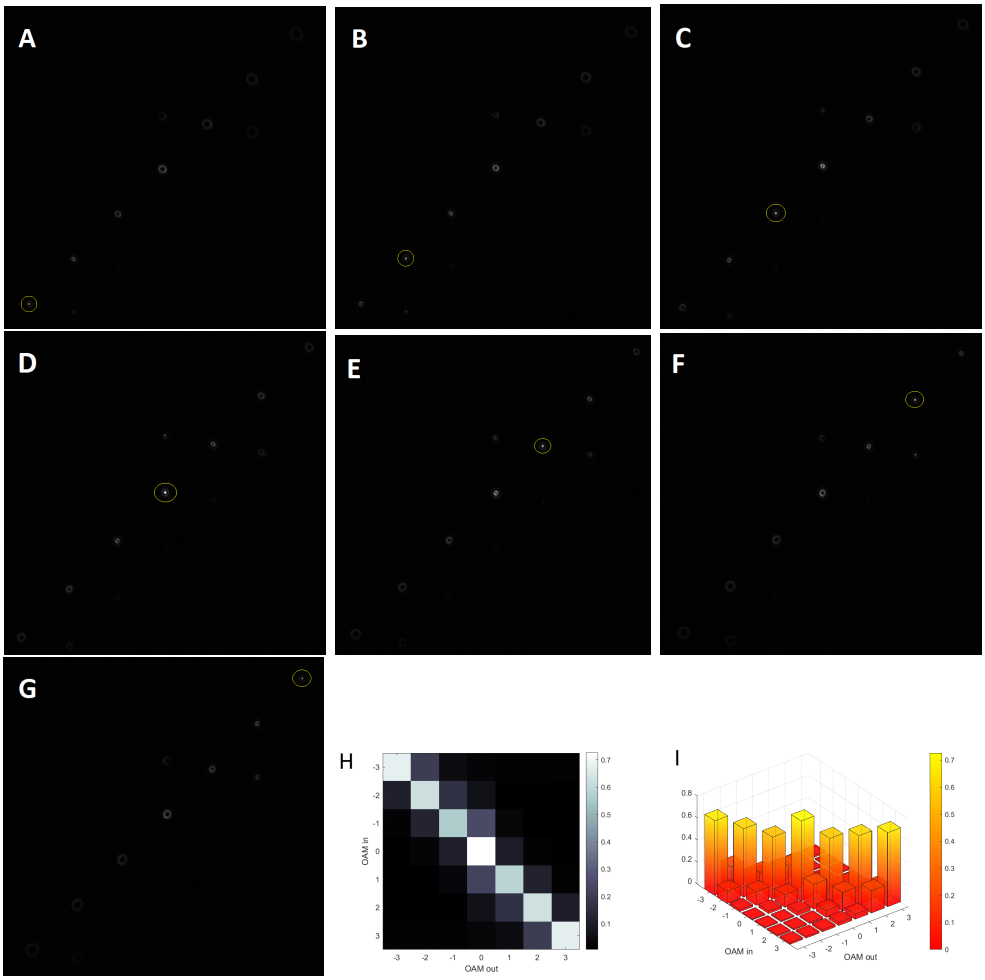

Figure 3.3: Bisector configuration: output for input m equal to -3(A), -2(B), -1(C), 0(D), 1(E), 2(F), 3(G) related to the pattern in figure 3.2 (the thin yellow circle surrounds the region in which the detector of the selected OAM beam is located), total intensity collected in the far-field in all the detectors, normalized to the total collected energy, plots in 2-dimension (H) and 3-dimension (I)

As shown in figure 3.2, the final output is comparable to a matrix of single detectors setted on a specific value of the topological charge. Once each of them is reached by the emerging beam, the combination of the setted m^* and the one of the incoming beam m results in a OAM mode of topological charge equal to their sum: when the result is equal to 0, a Gaussian peak appears in the corresponding spot, while the characteristic annular intensity is shown for the other channels. In the figure 3.3 the DCC images are collected in order to observe the shift of the peak while changing the topological charge m of the incoming beam. Integrating over the small area in which the intensity peak is centred, it is possible to obtain the intensity collected

by each channel; by normalizing it to the total energy, an efficiency of the procedure around 60% is calculated. The corresponding plots are shown in figure 3.3(h,i).

- **Spiral configuration**
  The same procedure has been repeated changing the spatial configuration into a spiral.

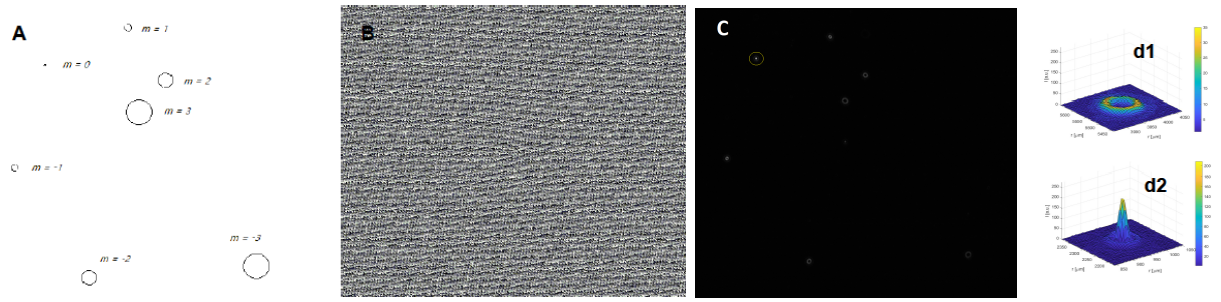

Figure 3.4: spiral configuration model(A), designed DOE(B), DCC image (C), 3D plots of a hole (d1) and a peak(d2) corresponding to the presence or not of the target OAM beam, respectively. The thin yellow circle surrounds the region in which the detector of the selected OAM beam is located.

The DCC images, one for each value of $m = [-3; 3]$ of the incoming OAM beam, are shown in the following figure.

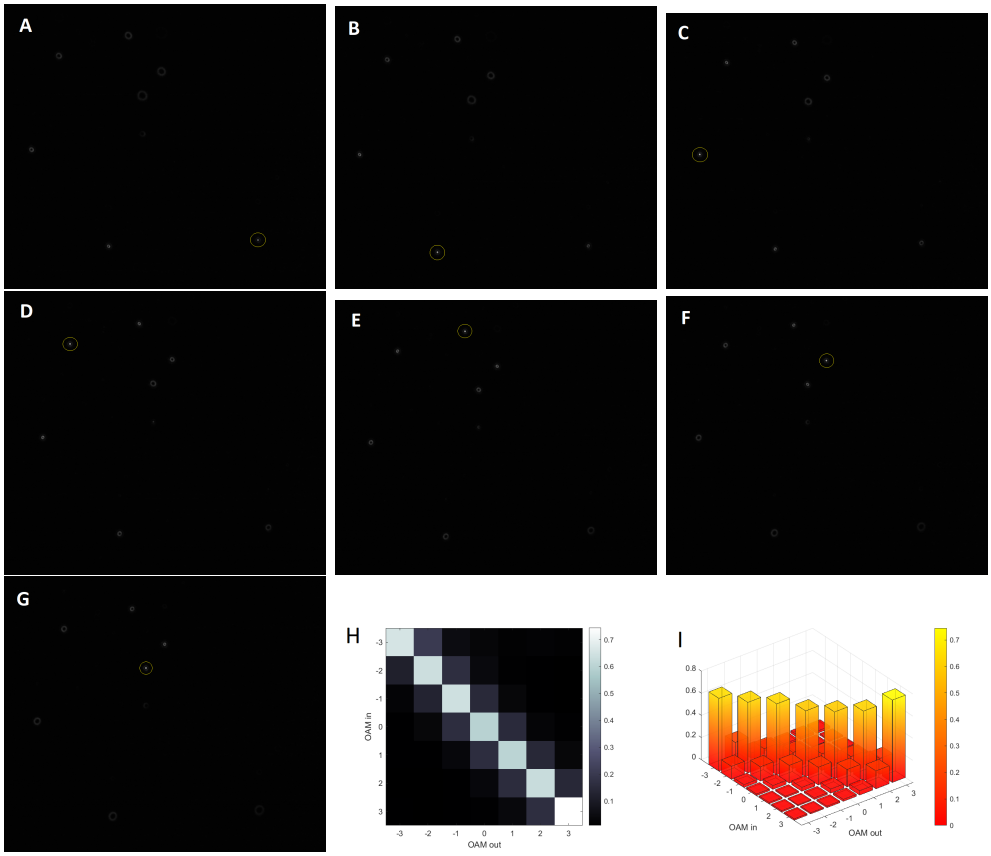

Figure 3.5: Spiral configuration: output for input m equal to -3(A), -2(B), -1(C), 0(D), 1(E), 2(F), 3(G) related to the pattern in figure 3.4, total intensity collected in the far-field in all the detectors, normalized to the total collected energy, plots in 2-dimension (H) and 3-dimension (I). The thin yellow circle surrounds the region in which the detector of the selected OAM beam is located.

In the same way, the total intensity collected by each channel is plotted in order to have an approximation of the efficiency. To conclude, the cross-talk (XT) of the channel corresponding to a given value of m is defined as:

$$XT_{m=m^*} = 10 \cdot log_{10} \frac{I^*}{I_{TOT}}$$

in which I^* is the sum at a fixed m^* of all the intensities when all the channels are on, except for that corresponds to m^*, while I_{TOT} is the total intensity collected by a specific channel when all the channels are used, m^* included.

Cross-talk

configuration	XT[dB]
bisector	-4.79 ± 0.54
spiral	-4.66 ± 0.40

The cross-talk is a negative value that represents the efficiency of the process and the isolation of the channels. The goal is that of decreasing this value, in order to have the maximum intensity collected in the corresponding channel.

Due to the overlap between the area of integration and the surrounding rings out of the intensity peak, there is always a small part of the OAM mode that is diffracted and detected in the other channels. In order to avoid this, the more suitable spatial configuration has to be designed.

3.2.3 Selection of the number of channels

As seen, it is possible to select an interval of values for the topological charge and then, the control of the configuration in the spatial distribution of the spots can be implemented. It is possible to repeat the same procedure with a greater number of channels. In the specific, this has been done with topological charge values in the interval of $m = [-5; 5]$ for a total of 11 channels. In this case the spots have been placed in a configuration consisting of two concentric circles.

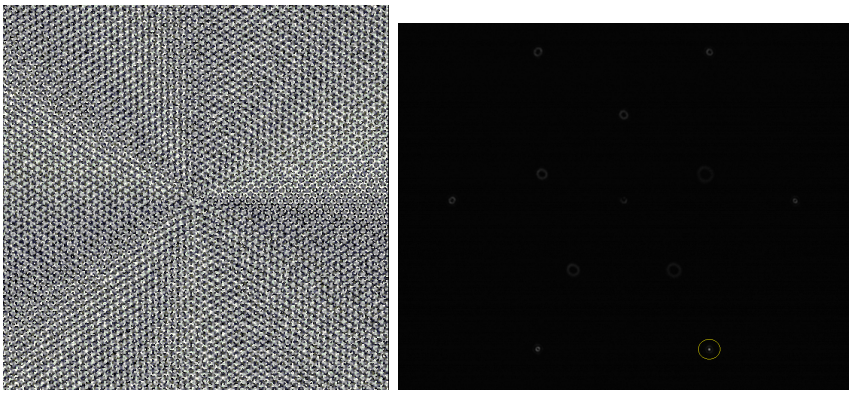

(a) DOE (b) DCC image

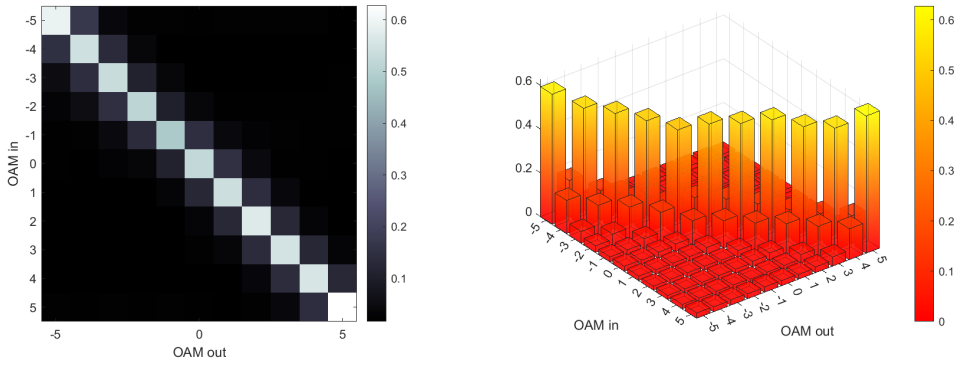

(c) Total intensity 2D plot (d) Total intensity 3D plot

Figure 3.6: holographic OAM-analyser for 11 channels. Designed DOE (a), DCC image of the output for $m = -2$ (b), total intensity collected in the far-field in all the detectors, normalized to the total collected energy, plots in 2-dimension (c) and 3-dimension (d). The yellow circle surrounds the region in which the detector of the selected OAM beam is located.

Due to the limited area over which the beam is detected in the far-field, an increasing number of channels is translated into a loss in efficiency. In terms of Cross-talk, in this case a value of $XT = (-3.49 \pm 0.13)dB$ is calculated: comparing it with the results of the previous section, a worsening in the efficiency is revealed.

3.2.4 Choice of the topological charge values

One way to improve the cross-talk, which means to reduce it, is to increase the separation between OAM modes in term of topological charge. Designing a diffractive optical element in order to detect OAM modes with $m = [-3; 3]$ with an interval $\Delta m = 1$ implies a possible superposition of spurious contributions from nearest-neighbours OAM values, as seen above. In the following, holographic sorter with different intervals Δm are exposed.

- $\Delta m = 1$

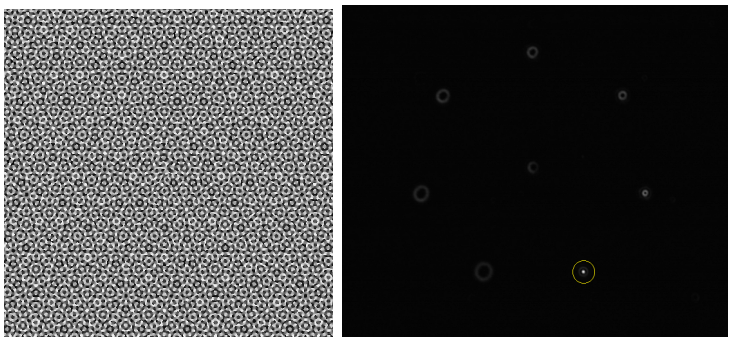

(a) DOE (b) DCC image

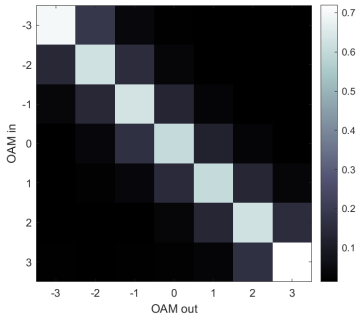

(c) Total intensity 2D plot

- $\Delta m = 2$

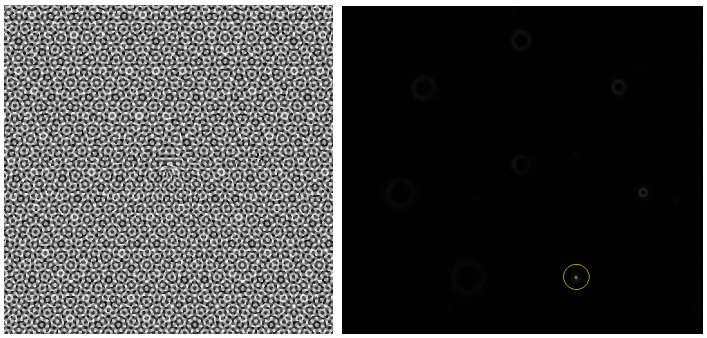

(d) DOE (e) DCC image

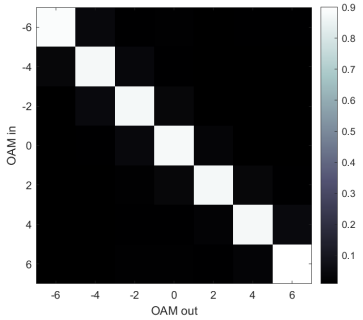

(f) Total intensity 2D plot

- $\Delta m = 3$

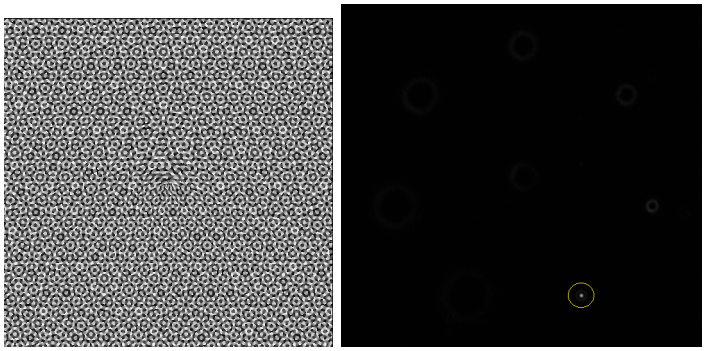

(g) DOE (h) DCC image

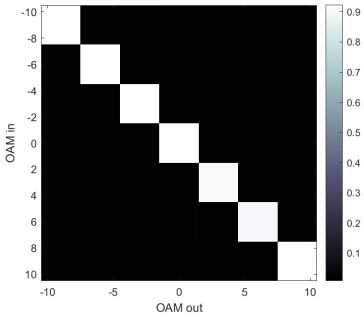

(i) Total intensity 2D plot

Figure 3.7: holographic OAM-analyser for $\Delta m = 1, 2, 3$. Designed DOE (a), DCC image of the output for $m = n\Delta m$, with $n = 1, 2, 3$ respectively (b), total intensity collected in the far-field in all the detectors, normalized to the total collected energy, plots in a 2-dimensional matrix (c). The yellow circle surrounds the region in which the detector of the selected OAM beam is located.

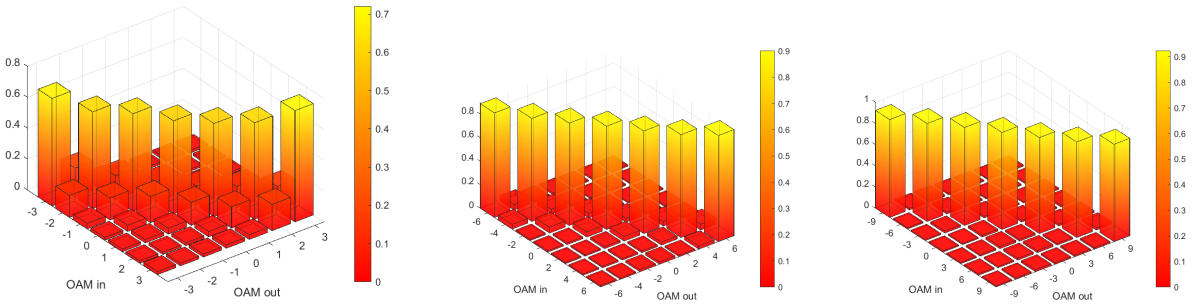

Figure 3.8: 3D matrices with collected intensity for each channel, normalized to the total energy

Cross-talk	
configuration	XT[dB]
$\Delta m = 1$	-4.57 $\pm$ 0.31
$\Delta m = 2$	-9.09 $\pm$ 0.26
$\Delta m = 3$	-10.8 $\pm$ 0.22

It is noticed straightforwardly how the efficiency increases, looking at the matrices containing the information on the total intensity collected by each channel, in particular, as shown in the following figure. To quantify the improvements, the cross-talk is computed and a graphic comparison is possible as indicated in figure 3.9.

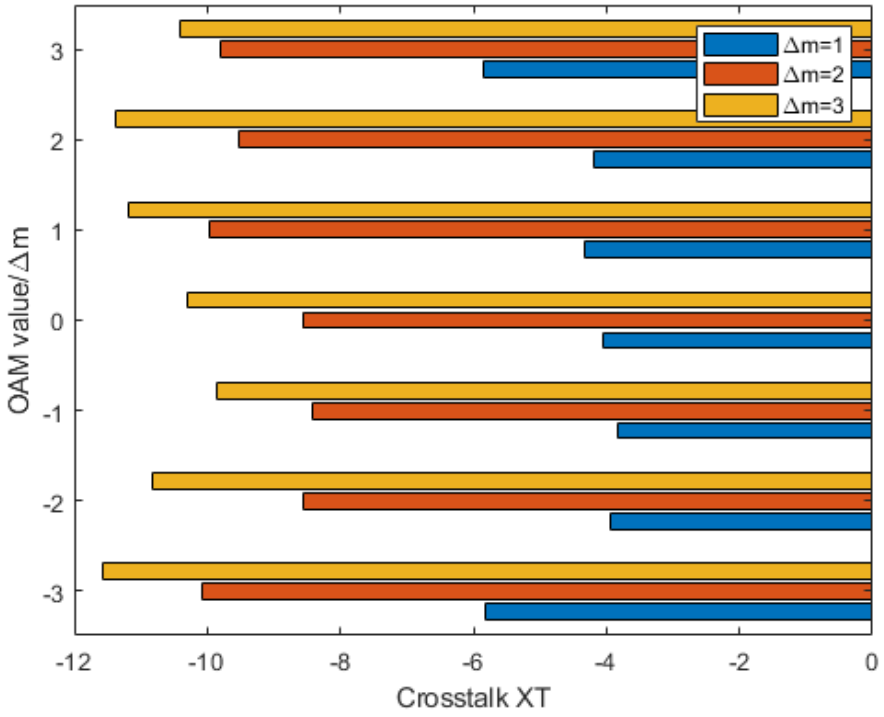

Figure 3.9: For the configurations shown in figure 3.7 the values of the Cross-talk for different Δm are grouped for each channel ($OAMvalue/\Delta m$).

Conclusions

In this thesis the attention has been focused on the generation and detection of beams carrying orbital angular momentum. Starting from the principles of wave and beam optics, the paraxial Helmholtz equation and its more useful solutions have been discussed in order to underline the features that characterize vortex beams, in general.

At this point, having the required theoretical knowledge, it has been possible to implement computational codes in *MATLAB* in order to design diffractive optical elements to generate optical vortex beams. An experimental setup based on SLMs has been arranged in order to visualize and analyse OAM modes. As predicted, the generated beams at variable values of the topological charge presented the characteristic annular intensity distribution confirming the existence of an optical vortex on the optical axis of the beam. By means of interferometric measurements, the helicoidal wavefronts have been underlined, proving one more time the theoretical predictions.

Structured light covers an important role in the context of telecommunication. In particular, (de) multiplexing techniques have been developed in order to satisfy the increasing demand in terms of bandwidth. One of this technique has been discussed in detail in this thesis: the mode-division multiplexing. Different OAM-mode analyzers have been implemented in order to study the possible degrees of freedom that can be manipulated in the view of improving the efficiency of this procedure. Due to spurious contributions from nearest-neighbours OAM values, it's necessary to find some ways to separate OAM beams in terms of spatial distribution and topological charges. In the specific, significant improvements have been seen taking topological charges with increasing Δm. More advanced techniques consists in combining OAM-MDM and SDM demultiplexing considering only the phase-pattern zone where the incident field is non-null; in this way, it's possible to use the remaining space for different phase pattern in order to form a multi-ring DOE with different phase levels [14]. SLMs play an important role in modelling different phase patters and to generate various classes of beams by means of a single device. Once the desired results are obtained, the elements can be fabricated with lithographic techniques as diffractive optics or metasurfaces [15].

To conclude, a quick overview of the more relevant applications is considered. Once laser beams carrying orbital angular momentum could be engineered, they found a large number of applications in a wide range of fields like microscopy, astronomy, communications, quantum information, etc.

- communications in free space: as seen in chapter 3, high dimensionality of OAM states space is relevant in information precessing and communication tasks. In this view, researches are focused on extending the actual applications to different regions of the spectrum and, in particular, longer wavelengths [16].

- imaging: due to the particular annular intensity distribution, OAM beams are used in advanced researches in astronomy, to implement new techniques for the identification of objects against bright background [17], in microscopy, to develop new models of microscope with higher resolution [18]. Furthermore, OAM beams can be used to reconstruct 3D images from a single scan of the sample [19].

- quantum information: due to the peculiarity of having a basis of an infinite number of orthogonal OAM states, a high dimensional state space is accessible to photons opening to new applications

in the field of cybersecurity (QKD) [7], and it is possible to entangle photons both in spin and OAM [3].

- trapping particles: it consists in the possibility to transfer separately spin or orbital angular momentum to a trapped particle causing a rotation around its centre owing to spin angular momentum, or around the centre of the beam owing to orbital angular momentum. This led to a wide use of angular momentum of light in the field of optical micromanipulation and trapping [20]

Bibliography

[1] J. F. Nye and M. V. Berry. Dislocations in Wave Trains. *Proceedings of the Royal Society of London Series A*, 336(1605):165–190, January 1974.

[2] L. Allen, M. W. Beijersbergen, R. J. C. Spreeuw, and J. P. Woerdman. Orbital angular momentum of light and the transformation of laguerre-gaussian laser modes. *Phys. Rev. A*, 45:8185–8189, Jun 1992.

[3] Mario Krenn, Mehul Malik, Manuel Erhard, and Anton Zeilinger. Orbital angular momentum of photons and the entanglement of laguerre–gaussian modes. *Philosophical Transactions of the Royal Society A: Mathematical, Physical and Engineering Sciences*, 375(2087):20150442, feb 2017.

[4] A. Ashkin, J. M. Dziedzic, J. E. Bjorkholm, and Steven Chu. Observation of a single-beam gradient force optical trap for dielectric particles. *Opt. Lett.*, 11(5):288–290, May 1986.

[5] M. Ritsch-Marte. Orbital angular momentum light in microscopy. *Philosophical Transactions of the Royal Society A: Mathematical, Physical and Engineering Sciences - Volume 375, Issue 2087.*

[6] Nenad Bozinovic, Yang Yue, Yongxiong Ren, Moshe Tur, Poul Kristensen, HAO HUANG, Alan Willner, and Siddharth Ramachandran. Terabit-scale orbital angular momentum mode division multiplexing in fibers. *Science (New York, N.Y.)*, 340:1545–8, 06 2013.

[7] Mohammad Mirhosseini, Omar S Magaña-Loaiza, Malcolm N O'Sullivan, Brandon Rodenburg, Mehul Malik, Martin P J Lavery, Miles J Padgett, Daniel J Gauthier, and Robert W Boyd. High-dimensional quantum cryptography with twisted light. *New Journal of Physics*, 17(3):033033, mar 2015.

[8] Robert Devlin, Antonio Ambrosio, Noah Rubin, J. Mueller, and Federico Capasso. Arbitrary spin-to-orbital angular momentum conversion of light. *Science*, 358:eaao5392, 11 2017.

[9] M. V . Vasnetsov M. S. Soskin, V. Yu. Bazhenov. Laser beams with screw dislocations in their wavefronts. 52:1037.

[10] M.W. Beijersbergen, L. Allen, H.E.L.O. van der Veen, and J.P. Woerdman. Astigmatic laser mode converters and transfer of orbital angular momentum. *Optics Communications*, 96(1):123–132, 1993.

[11] M.W. Beijersbergen, R.P.C. Coerwinkel, M. Kristensen, and J.P. Woerdman. Helical-wavefront laser beams produced with a spiral phaseplate. *Optics Communications*, 112(5):321–327, 1994.

[12] Lorenzo Marrucci, Ebrahim Karimi, Sergei Slussarenko, Bruno Piccirillo, Enrico Santamato, Eleonora Nagali, and Fabio Sciarrino. Spin-to-orbital conversion of the angular momentum of light and its classical and quantum applications. *Journal of Optics*, 13(6):064001, apr 2011.

[13] D. J. Richardson, J. M. Fini, and L. E. Nelson. Space-division multiplexing in optical fibres. *Nature Photonics*, 7(5):354–362, May 2013.

[14] Gianluca Ruffato, Michele Massari, and Filippo Romanato. Diffractive optics for combined spatial- and mode- division demultiplexing of optical vortices: design, fabrication and optical characterization. *Scientific Reports*, 6, 2016.

[15] Wei Wang, Yan Li, Zhongyi Guo, Rongzhen Li, Jingran Zhang, Anjun Zhang, and Shiliang Qu. Ultra-thin optical vortex phase plate based on the metasurface and the angular momentum transformation. *Journal of Optics*, 17(4):045102, mar 2015.

[16] Fabrizio Tamburini, Elettra Mari, Anna Sponselli, Bo Thidé, Antonio Bianchini, and Filippo Romanato. Encoding many channels on the same frequency through radio vorticity: first experimental test. *New Journal of Physics*, 14(3):033001, mar 2012.

[17] Grover A. Swartzlander, Erin L. Ford, Rukiah S. Abdul-Malik, Laird M. Close, Mary Anne Peters, David M. Palacios, and Daniel W. Wilson. Astronomical demonstration of an optical vortex coronagraph. *Opt. Express*, 16(14):10200–10207, Jul 2008.

[18] Dominik Wildanger, Johanna Bückers, Volker Westphal, Stefan W. Hell, and Lars Kastrup. A sted microscope aligned by design. *Opt. Express*, 17(18):16100–16110, Aug 2009.

[19] Alexander Jesacher, Monika Ritsch-Marte, and Rafael Piestun. Three-dimensional information from two-dimensional scans: a scanning microscope with postacquisition refocusing capability. *Optica*, 2(3):210–213, Mar 2015.

[20] Lynn Paterson, M. P. Macdonald, Jochen Arlt, Wilson Sibbett, Peter E. Bryant, and Kishan Dholakia. Controlled rotation of optically trapped microscopic particles. *Science*, 292:912 – 914, 2001.